SI MATERIALS AND METHODS

Protein Overexpression, Purification, and Reconstitution. ELIC was overexpressed and purified using undecyl-β-maltoside (UDM) as the detergent as previously described (1,2). Purified ELIC was reconstituted into POPC (Avanti Polar Lipids) nanodiscs using the the membrane-scaffolding protein MSP1E3D1 following established protocols (3). ELIC-containing nanodiscs were separated from empty ones by passing the mixture through a Ni-NTA column (ThermoFisher Scientific). In the absence of imidazole, ELIC-containing nanodiscs bound to the resin (perhaps through the di-histidine motif in the M3–M4 linker), whereas empty nanodiscs did not; ELIC-containing nanodiscs eluted in 30-mM imidazole. Purified ELIC was reconstituted into POPC or asolectin (Cat. # 11145; Sigma) cell-sized proteoliposomes following the "dehydration-rehydration" method (4,5). First, thoroughly dried lipids were dispersed until clarity at a concentration of 10 mg/mL using a probe sonicator (Branson) set at minimum output power. For asolectin, the dispersion solution was (in mM) 150 NaCl and 10 sodium phosphate, pH 8.0. For POPC, the dispersion solution was (in mM) 5 HEPES/KOH, pH 7.4. These small liposomes were mixed with detergent-purified ELIC at a protein-to-lipid ratio that ranged between 1:20 and 1:40 (by weight) and the detergent was adsorbed onto Bio-Beads™ SM-2 resin (Bio-Rad) to form small proteoliposomes. The small proteoliposomes were sedimented by ultracentrifugation at 30,000 rpm (rotor Type 50.2 Ti; Beckman Coulter), and the pellets were resuspended at a concentration of 100 mg of lipid/mL (using the same solution as that used for dispersion), aliquoted, and stored at –80°C. Thawed aliquots were placed on poly-L-lysine-coated glass coverslips (2.5 μL per coverslip) and dried overnight at 4°C under vacuum in a dessicator containing Drierite granules (W. A. Hammond Drierite Company). The dried lipid-protein mixtures were rehydrated at 4°C by placing the coverslips inside closed Petri dishes lined with wet filter-paper pads; 20 μL of rehydrating solution were added to each coverslip. For asolectin–ELIC mixtures, the rehydration solution was (in mM) 150 NaCl and 10 sodium phosphate, pH 8.0, whereas for POPC–

ELIC mixtures, the rehydration solution was (in mM) 5 KCl, 1 $CaCl_2$, 250 mannitol, and 5 HEPES/KOH, pH 7.4 (6). Electrophysiological experiments started ~30 hr later. During rehydration, cell-sized multillamelar and unilamellar structures formed from a mostly amorphous mass of lipid and protein.

Electrophysiology. Currents from ELIC-incorporated cell-sized proteoliposomes and from transiently-transfected HEK-293 cells were recorded in the inside-out and whole-cell patch-clamp configurations, respectively, at ~22°C with an effective bandwidth of DC–5 kHz using an Axopatch 200B amplifier (Molecular Devices). Currents were digitized at 100 kHz, and for display in figures, they were decimated by a factor of 100. Data were acquired and analyzed using pCLAMP 9.2 software (Molecular Devices). The reference Ag/AgCl wire was connected to the extracellular solution through an agar bridge containing 200-mM KCl. In the whole-cell configuration, series-resistance compensation was used and set to ~80%. Agonist-concentration jumps were applied using a piece of double-barreled glass "θ-tubing" (7). The flow of solution through the θ-tube was controlled using a gravity-fed system (ALA BPS-8; ALA Scientific Instruments), and the movement of the θ-tube was achieved using a piezo-electric arm (Burleigh-LSS-3100; discontinued) controlled by pCLAMP 9.2 software and a Digidata 1322A interface (Molecular Devices). Signals from this interface were low-pass filtered (900C; Frequency Devices) at a cutoff frequency of 5–15 Hz prior to their arrival at the piezoelectric arm to reduce ringing in the θ-tube motion. The relative positioning of the θ-tube and the patch pipette was adjusted so as to optimize the perfusion of either the excised patch or the entire cell. During whole-cell recordings, the "patched" cell remained attached to a glass coverslip placed at the bottom of the recording chamber. In the excised-patch configuration, our gravity-fed perfusion system achieved a solution-exchange time of ~0.7–1.5 ms for the $t_{10–90\%}$ and ~1.5–4.5 ms for the $t_{90–10\%}$, whereas in the whole-cell configuration, these values were ~5–10 ms for both the $t_{10–90\%}$ and $t_{90–10\%}$, as estimated from changes in the liquid-junction current measured with an open-tip patch pipette.

Although slower than pressurized perfusion, we chose to use a gravity-fed system, here, because it was gentler on the seals and because it was not our intention to perform a detailed characterization of the kinetic aspects of channel function. In the inside-out configuration, the pipette solution was (in mM) 142 KCl, 5.4 NaCl, 1.8 $CaCl_2$, 1.7 $MgCl_2$, and 10 HEPES/KOH, pH 7.4. In the whole-cell configuration, the pipette solution was (in mM) 110 KCl, 40 KF, and 5 HEPES/KOH, pH 7.4. For both configurations, the bath solution was (in mM) 5 KCl, 250 mannitol, and 5 HEPES/KOH, pH 7.4. The two extracellular solutions applied through the θ-tube barrels were bath solution with and without 1 or 10-mM propylammonium-chloride/propylamine. At pH 7.4, the concentration of propylammonium cation ($pK_a \cong 10.71$) in a 1-mM solution of the salt/base mixture can be calculated to be 0.9995 mM, and that in a 10-mM solution of the mixture, 9.995 mM. In a subset of patch-clamp recordings from POPC-ELIC proteoliposomes, the agonist was also added to the pipette solution. Seals between proteoliposomal membranes and patch-clamp micropipettes (borosilicate glass; Corning 7740; Sutter Instruments) were typically leakier and more fragile for POPC than they were for asolectin. In the case of POPC, we also noted a marked tendency of the membrane to creep up the pipette interior to the extent that, frequently, proteoliposomes were "swallowed" completely upon the application of negative suction.

Cryo-EM Data Collection and Processing. Unliganded and propylammonium-bound ELIC cryo-EM grids were prepared using Spotiton 1.0 (8). Nanowire 300 mesh carbon or gold lacey grids, prepared in house, were plasma-cleaned with O_2 and H_2 for 10 secs using a Solarus plasma cleaner (Gatan). 5 μL of protein sample were aspirated by the Spotiton piezo tip, and about 80 × 50 pL of sample were spotted onto the grid as it passed the piezo tip en route to being plunged into liquid ethane. All images were acquired by a Titan Krios microscope (ThermoFisher Scientific) operated at 300 kV using a Gatan K2 direct electron detector (Gatan) with an energy filter and in counting mode. Images were automatically acquired using Leginon (9) and were pre-processed using software integrated into the

Appion pipeline (10). Frames were aligned using MotionCor2 software with dose weighting (11), and particles were picked and extracted automatically using DoGpicker (12). Particle stacks were then imported into RELION2.1 (13) and were processed through several rounds of 2D and 3D classification. Selected classes were then processed for high-resolution 3D refinement (Table S1). Examples of cryo-EM micrographs and 2D class averages of unliganded and agonist-bound ELIC are shown in Figs. S2A–C and S3A–C, respectively. The final resolution was estimated using Fourier Shell Correlation in RELION 2.1 using a 0.143 cut-off threshold (Fig. S2D and S3D). Cryo-EM data collection and processing statistics are listed in Table S1.

Cryo-EM Atomic-model Building. Model building for unliganded and propylammonium-bound ELIC was performed in two steps. First, the structure factors obtained from the EM maps (by using Phenix.map_to_structure_factors) and primary sequence of ELIC were used as input in BALBES (14), and the output coordinate file was used for model building and refinement. The manual adjustment of the models inside the map and the subsequent refinement was done using Coot (15) and phenix_real_space_refine (16,17) iteratively. Model-building and refinement cycles were performed until no further improvement in cross-correlation (16,17) and Molprobity scores (18) was observed. The second step involved the use of molecular dynamics flexible fitting (MDFF; refs. 19–21) to build the model in those regions that were difficult to fit manually. The best-fitted regions from the two approaches were combined and further refined (16,17) to obtain the final atomic models. As validation tools for the plausibility of the latter, we computed map-*versus*-model cross-correlation values (CC; refs. 16,17), a variety of parameters from MolProbity (18), EM ringer scores (22), and map-*versus*-model FSC-threshold crossings (Figs. S2E and S3E). The corresponding values are listed in Table S1.

Molecular Dynamics Flexible Fitting. The starting structures for both the unliganded and propylammonium-bound models were taken from a crystal structure of ELIC (PDB ID: 2VL0; ref. 1). Owing to the different protein sequences, SWISS-MODEL (23,24) was used to insert the additional

residue Gly 164. For building half-map structural models, resolution-exchange MDFF simulations (ReMDFF; refs. 19–21) were performed using NAMD 2 (25). CHARMM36m parameters (26) were used for the protein, and the parameters for propylammonium were obtained from the CGenFF server (27–29). Instead of using Gaussian-blurred grid potentials from the original ReMDFF method (20), a new protocol was used here where each successive grid potential was processed through low-pass filtering to avoid the merging of densities of nearby transmembrane helices. Three grid potentials were used based on the original cryo-EM maps along with low-pass-filtered maps with spatial-frequency thresholds of 5 Å and 10 Å. Each ReMDFF simulation started with a 500-step energy minimization using the conjugate gradient with line-search algorithm (30). The systems were simulated at 300 K in an implicit solvent using the Generalized-Born method (31,32) at an implicit ionic strength of 150 mM. The temperature was maintained using the Langevin algorithm (33) with a damping coefficient of 1 ps^{-1}. The total ReMDFF simulation time was 1 ns with an exchange attempt every 2 ps. After ReMDFF, the sampled conformation with the highest cross-correlation to the original cryo-EM map was selected. An additional simulated-annealing simulation was performed on the chosen conformation where an initial 1,000-step energy minimization was performed, followed by an annealing simulation in which the temperature dropped 1 K every 2 ps (from 300 K to 0 K), as well as a final 1,000-step energy minimization. The best conformations (as judged from cross-correlation coefficients) were chosen as the starting conformations for the full-map MDFF simulations, where only a grid potential corresponding to the unfiltered full map was used. For the propylammonium-bound state, owing to the missing densities for the M4 α-helices in the full map, harmonic restraints (k = 1 kcal mol^{-1} $Å^{-2}$) were applied to the backbone heavy atoms of M4 residues (residues 303–317).

Molecular Dynamics. Each system was solvated and ionized with 150-mM NaCl, and embedded in a pure POPC membrane (generated by CHARMM-GUI; ref. 34) using a previously published protocol (35). NAMD 2 (25) was used to perform all simulations. The force-field parameters for protein and

propylammonium were the same as those used for MDFF. The parameters for (neutral) propylamine were obtained from the CGenFF server (27–29). CHARMM36 force-field (36) was used for lipids. Corrections to the van der Waals interactions between Na^+ ions and lipids were applied (37). The final-system size was 180 Å × 180 Å × 210 Å with ~640,000 atoms. The Langevin temperature-control algorithm (33) was used to maintain an average temperature of 310 K. The Nosé-Hoover Langevin piston pressure-control algorithm (38,39) was used to keep the pressure at 101.325 kPa with a piston period of 200 fs, an oscillation decay time of 100 fs, and the ratio between the lengths along the *X* and *Y* dimensions constrained. All simulations were preceded by 3,000 steps of energy minimization. This was followed by 500 ps of simulation during which the protein-backbone heavy atoms, lipid-phosphorus atoms, and ligand heavy atoms were restrained to allow the lipid-tail-group atoms to relax. For the three simulations in Fig. S7, the restraining force constant was k = 10 kcal mol^{-1} Å^{-2} for the protein, lipid, and orthosteric-site-bound propylammonium, whereas k = 100 kcal mol^{-1} Å^{-2} for pore-lumen-bound propylammonium or propylamine. After this step, the restraints on lipid-phosphorus atoms were removed, and the simulations continued for 20 ns to allow the equilibration of the membrane. Over the following 10 ns (that is, during the 20.5–30.5-ns interval), the restraints were gradually reduced by a factor of 100 (from 10 kcal mol^{-1} Å^{-2} to 0.1 kcal mol^{-1} Å^{-2} and from 100 kcal mol^{-1} Å^{-2} to 1 kcal mol^{-1} Å^{-2}). Finally, at 30.5 ns, the restraints on heavy atoms of the protein backbone and propylammonium bound to the orthosteric sites were removed, whereas those applied on pore-lumen-bound propylammonium or propylamine remained at 1 kcal mol^{-1} Å^{-2}. The simulations continued for a total of 500 ns. For the three simulations in Figs. 7, 8, and S8, we removed the five molecules of propylammonium bound to the pore-lumen sites and followed, essentially, the same protocol as that described above for the simulations in Fig. S7. Here, the initial force constant was k = 10 kcal mol^{-1} Å^{-2} for all restrained atoms, and it was gradually reduced (during the 20.5–30.5-ns interval) by a factor of 100. At 30.5 ns, the restraints on heavy atoms of propylammonium were

removed, whereas those applied on the protein Cα atoms remained at 0.1 kcal mol^{-1} $Å^{-2}$. These simulations continued for a total of 500 ns.

Free-energy perturbation calculations. To estimate the difference in propylammonium affinities of the propylammonium-bound and unliganded atomic models of ELIC, we performed free-energy perturbation (FEP) calculations (40,41). For the propylammonium-bound model, the simulations started with the last frame of the 500-ns all-atom MD simulation presented in Fig. 7, whereas for the unliganded model, the simulations started with the last frame of the simulation presented in Fig. 8. In each case, the propylammonium molecule/binding-site displaying the smallest root-mean-square fluctuations (RMSF) during the last 450 ns of the corresponding all-atom simulation was chosen for the FEP calculation. To maintain the electrical neutrality of the simulation system during the annihilation of the ligand, one Cl^- (in solution) was annihilated simultaneously. The alchemical transformations were performed in both forward (λ increasing from 0 to 1; annihilation) and backward (λ decreasing from 1 to 0; creation) directions. A soft-core van der Waals radius-shifting coefficient of 5 Å was chosen. In the forward transformation (annihilation), the van der Waals interactions and the electrostatic interactions of the annihilated particles were linearly decoupled to the simulation over a λ range of 0–1 and 0–0.5, respectively, and in the backward transformation (creation), these interactions were linearly coupled to the simulation in the corresponding λ ranges, in the reverse direction. Each FEP alchemical transformation along the λ reaction path was stratified into 50 equally spaced consecutive windows to ensure a gradual transformation. Within each window, the simulation consisted of an equilibration phase of 100 ps and a subsequent 1-ns simulation for data collection at a frequency of one sample every 20 fs, resulting in an accumulated simulation time of 110 ns for each system. To prevent the dissociation of the ligand during the alchemical transformation, two types of restraints were applied to the annihilated propylammonium molecule in both systems: a) the distances from the Cδ atoms of Glu 77 and Glu 131 to the nitrogen atom of the propylammonium molecule were restrained to

remain below 4.2 Å, that is, the maximum value of these distances observed in the MD simulation of propylammonium-bound ELIC (Fig. 7); and b) the center-of-mass deviation of the ligand was positionally restrained to remain within 2 Å. The annihilated Cl^- was harmonically restrained with a force constant of 1 kcal mol^{-1} $Å^{-2}$, and the protein Cα atoms were harmonically restrained with a force constant of 0.1 kcal mol^{-1} $Å^{-2}$. Simulation parameters were the same as those described above for MD. The output of the FEP calculations was analyzed using the ParseFEP (42) plugin in VMD with statistical errors estimated using the implemented Bennett Acceptance Ratio (BAR) method (43).

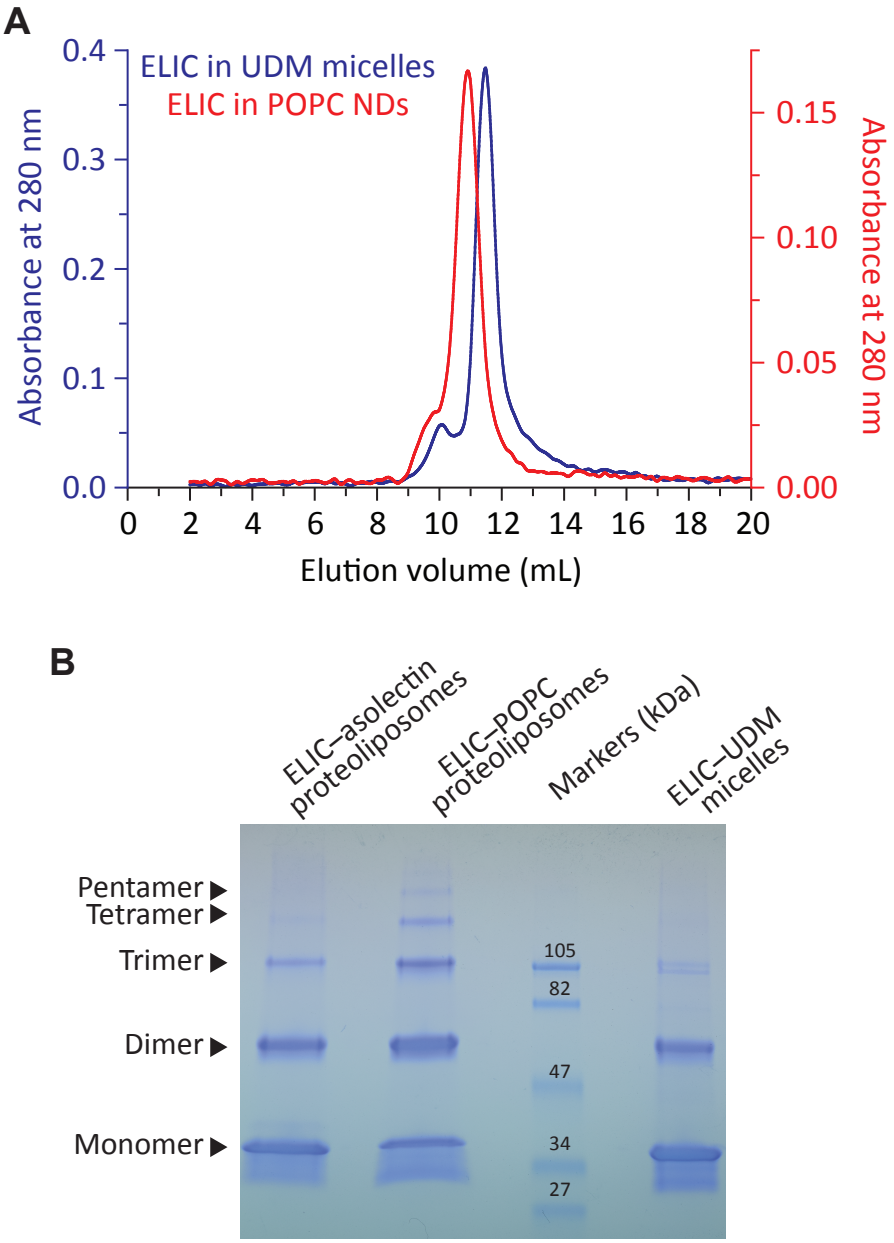

Fig. S1. ELIC reconstitution in lipid nanodiscs (NDs) and proteoliposomes. (*A*) Size-exclusion chromatography profiles. The eluate was collected in 0.5-mL fractions. In the case of UDM-solubilized ELIC, the three fractions containing and flanking the peak were taken for incorporation into nanodiscs or proteoliposomes. In the case POPC-embedded ELIC, only the fraction containing the peak was further processed for observation under the electron microscope. (*B*) SDS–polyacrylamide gel electrophoresis (SDS–PAGE) of the indicated samples. The molecular mass of ELIC, predicted from the polypeptide sequence, is ~37 kDa for each subunit. The same amount of proteoliposomes prepared at the same ELIC-to-lipid (mass-to-mass) ratio was loaded into the two leftmost lanes. All samples were heated at ~80°C for 10 min in a solution containing 4.5 % (w/v) SDS.

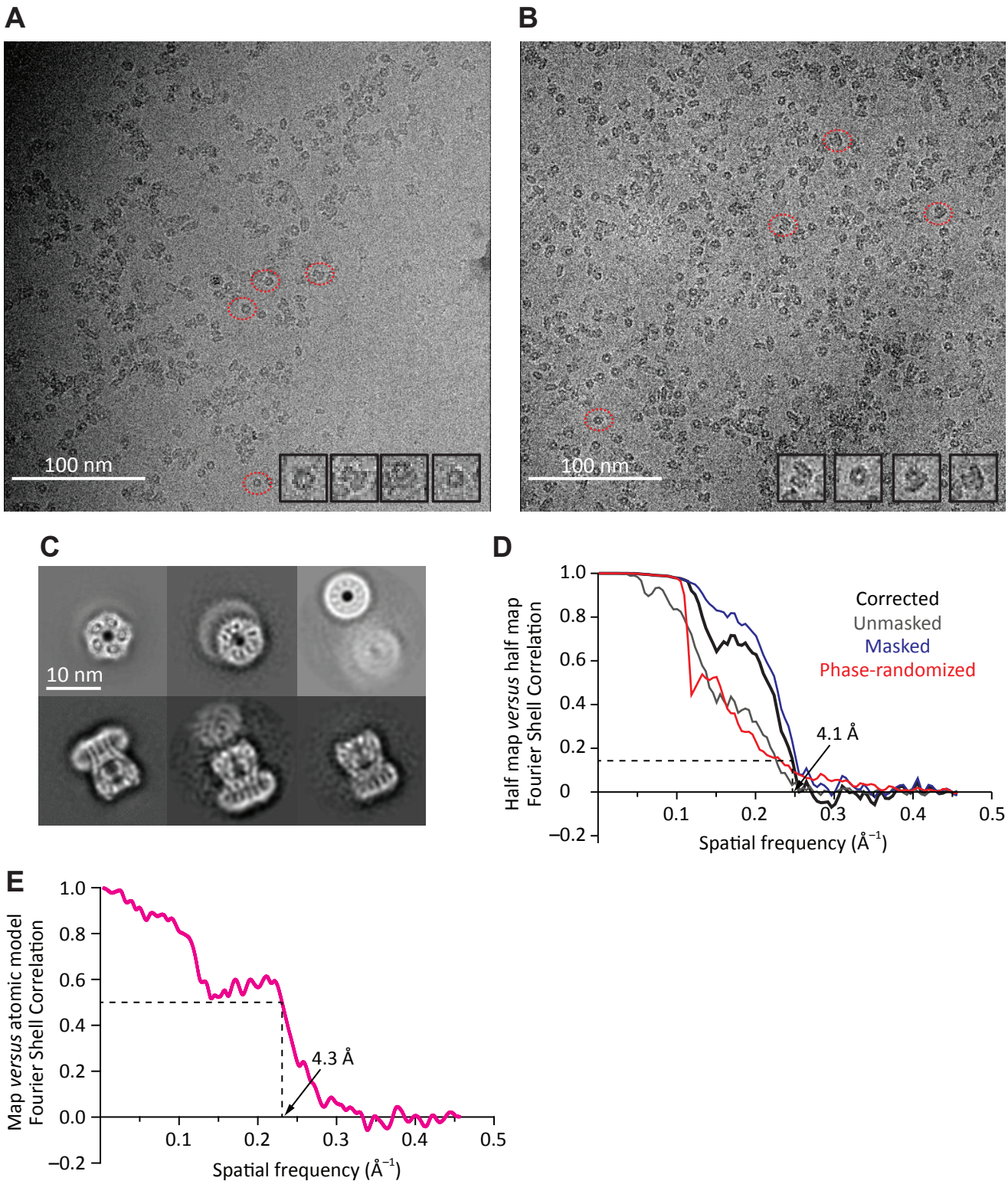

Fig. S2. Unliganded ELIC in POPC nanodiscs: cryo-EM micrographs, 2D class averages, and Fourier Shell Correlation (FSC) plots. (*A*, *B*) Example micrographs with defocus 1.57 µm (*A*) and 1.47 µm (*B*). (*C*) Selected 2D class averages generated in RELION2.1 (13) using the option to ignore CTFs until first peak. (*D*) FSC curves computed between independently refined "half maps" ("gold-standard" procedure) using RELION2.1 (13). Global resolution was estimated using the 1/7 (≈ 0.143) cut-off criterion (44). (*E*) FSC curve computed between the full experimental map and a noise-free map calculated from the fitted atomic coordinates using *Scipion* (45). A soft-edged, threshold-based mask was applied to the experimental map before computation of the FSC.

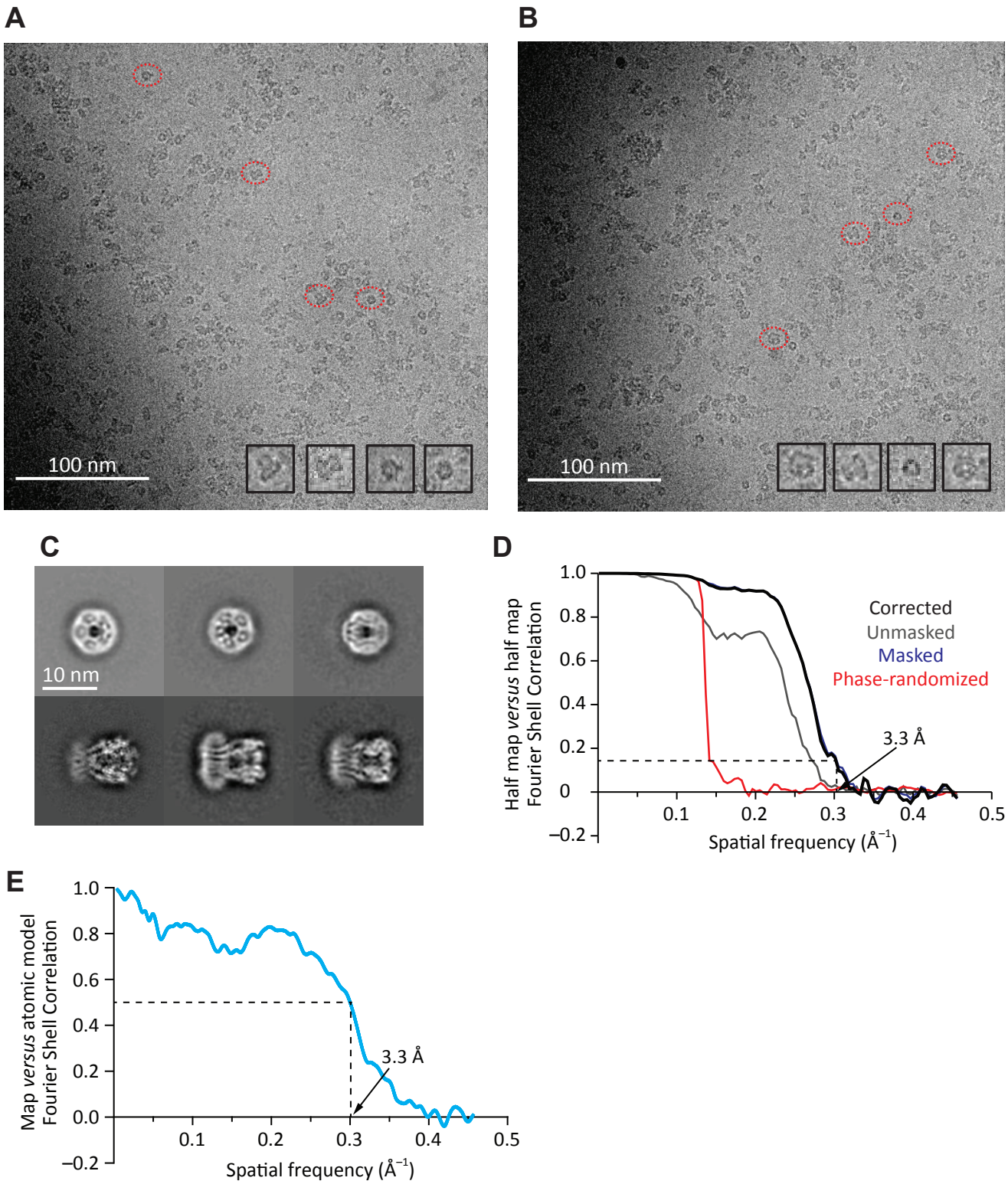

Fig. S3. Agonist-bound ELIC in POPC nanodiscs: cryo-EM micrographs, 2D class averages, and Fourier Shell Correlation (FSC) plots. (*A*, *B*) Example micrographs with defocus 1.96 µm (*A*) and 1.77 µm (*B*). (*C*) Selected 2D class averages generated in RELION2.1 (13) using the option to ignore CTFs until first peak. (*D*) FSC curves computed between independently refined "half maps" ("gold-standard" procedure) using RELION2.1 (13). Global resolution was estimated using the 1/7 (≈ 0.143) cut-off criterion (44). (*E*) FSC curve computed between the full experimental map and a noise-free map calculated from the fitted atomic coordinates using *Scipion* (45). A soft-edged, threshold-based mask was applied to the experimental map before computation of the FSC.

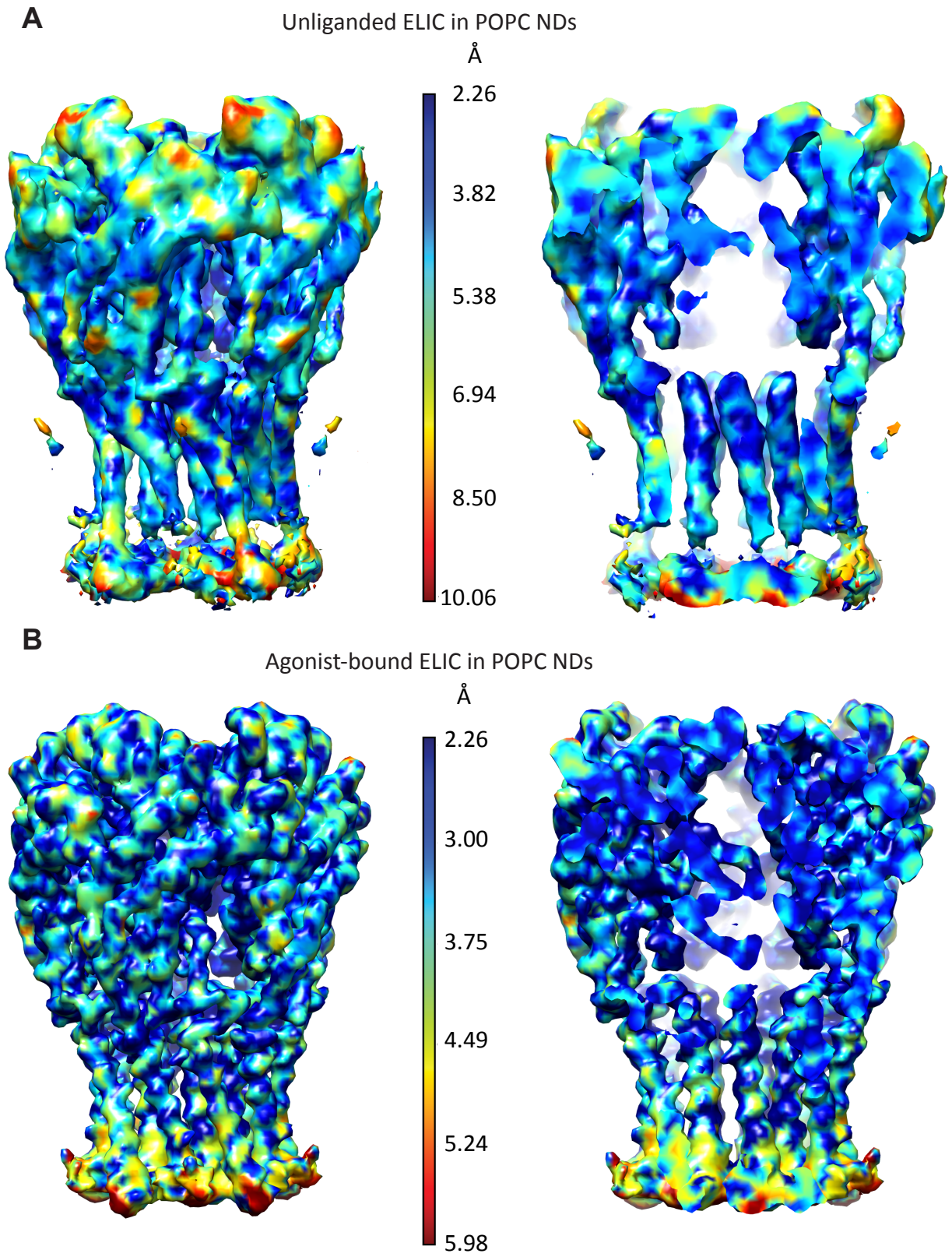

Fig. S4. Three-dimensional reconstructions colored according to local resolution. *A*) Full (*left*) and slice-through-the-center (*right*) views of unliganded ELIC. (*B*) Full (*left*) and slice-through-the-center (*right*) views of agonist-bound ELIC. For each reconstruction, the local resolution was estimated with *MonoRes/Scipion* (45,46) using the corresponding full (unfiltered and unsharpened) map and a 3D mask. The latter was created by thresholding the former in an attempt to exclude voxels occupied by protein, agonist molecules (if present), and nanodisc components from the noise-only volume. For clarity, the regions of density corresponding to the poorly resolved M4 segments and the nanodisc were omitted. NDs: nanodiscs.

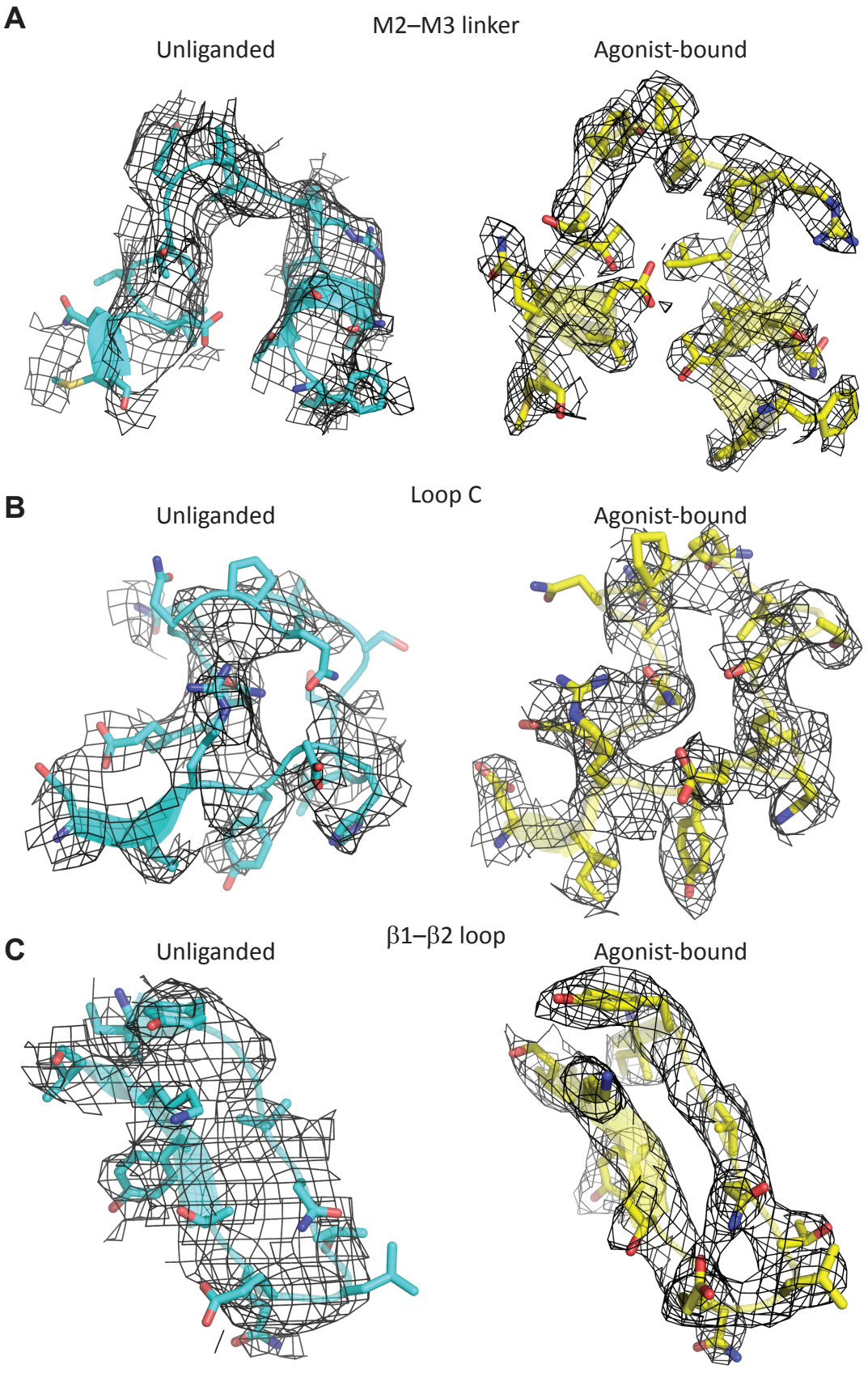

Fig. S5. Comparison of cryo-EM densities. Analysis of the unliganded and propylammonium-bound structural models of ELIC indicated that the M2–M3 linker, the most extracellular α-helical turn of M2, loop C (that is, the β9–β10 loop), and the β1–β2 loop differ the most between both models. (*A*) M2–M3 linker and extracellular ends of flanking α-helices (residues 247–265). Density-contour levels: 4.5 (unliganded) and 3.5 (agonist-bound). (*B*) Loop C and flanking β-strands (residues 172–187). Density-contour levels: 6.0 (unliganded) and 5.0 (agonist-bound). (*C*) β1–β2 loop and flanking β-strands (residues 23–35). Density-contour levels: 6.0 (unliganded) and 5.0 (agonist-bound). For all panels, the selected ELIC residues are displayed in ribbon and stick representations, and the cryo-EM density is displayed as a black mesh. Molecular images were prepared with PyMOL (47).

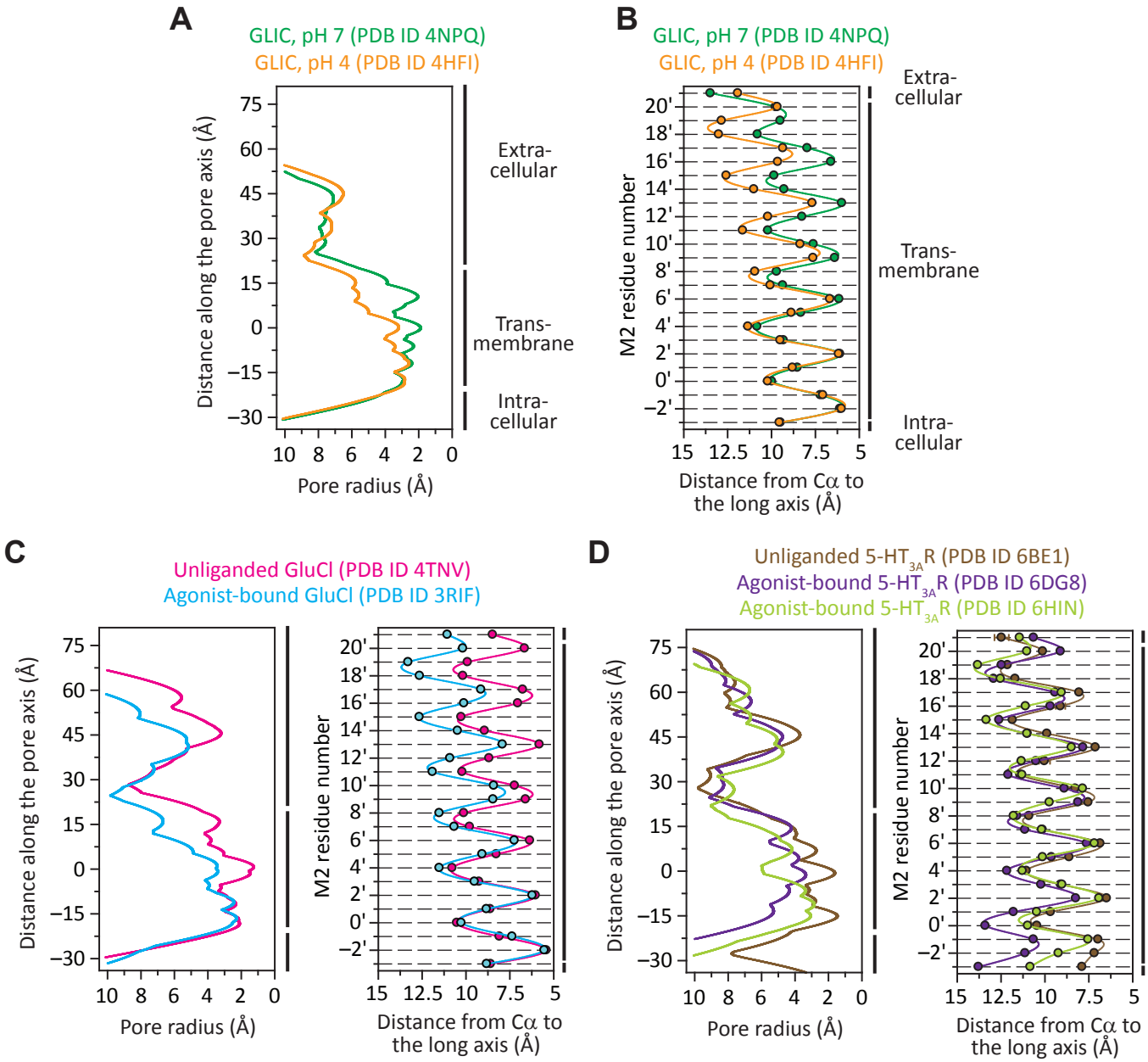

Fig. S6. Pore profiles. (*A*) Pore-radius profiles estimated using HOLE (48) for the indicated structural models of unliganded-closed and liganded-open GLIC. (*B*) Distances between the axis of ion permeation and the Cα atoms for residues in the pore-lining M2 α-helices (mean ± SE of all subunits; error bars smaller than the symbols were omitted) of the indicated models. (*C*) HOLE (left) and Cα (right) profiles of the indicated models of unliganded-closed and liganded-open GluCl. (*D*) HOLE (left) and Cα (right) profiles of the indicated models of unliganded-closed and liganded-open 5-HT$_{3A}$R. For all HOLE profiles, the zero value along the *y*-axis corresponds to the mean position of all five Leu 240 (position 9′) Cα atoms along the axis of ion permeation. For all Cα profiles, M2 residues are denoted using the prime-numbering system.

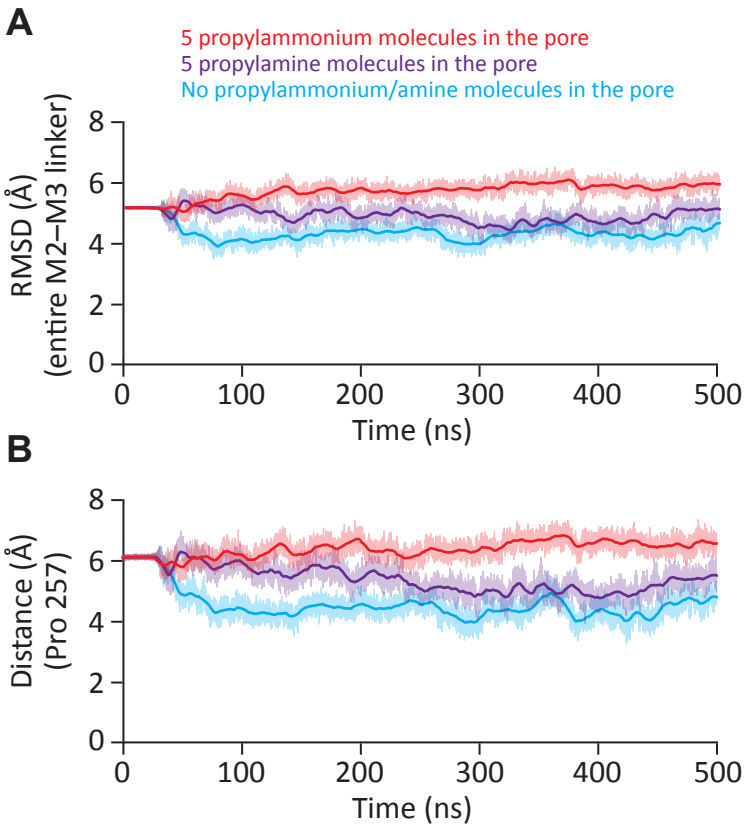

Fig. S7. All-atom MD simulations starting with the agonist-bound atomic model of ELIC under three different pore-lumen conditions. (*A*) Root-mean-square deviation (RMSD) of Cα atoms in the M2–M3 linker (residues 253–260) of the simulated models relative to those in the unliganded atomic model, averaged over all five subunits. (*B*) Distance between the Cα atom of Pro 257 in the simulated models and that in the unliganded atomic model, averaged over all five subunits. Pro 257 is the M2–M3-linker residue whose Cα-atom coordinates differed the most (~6 Å) upon a global superposition of whole pentameric models of unliganded and agonist-bound ELIC. For both panels, distances were calculated every 10 ps and are diplayed as thin lines; thick lines represent moving averages. The color code is the same for both panels.

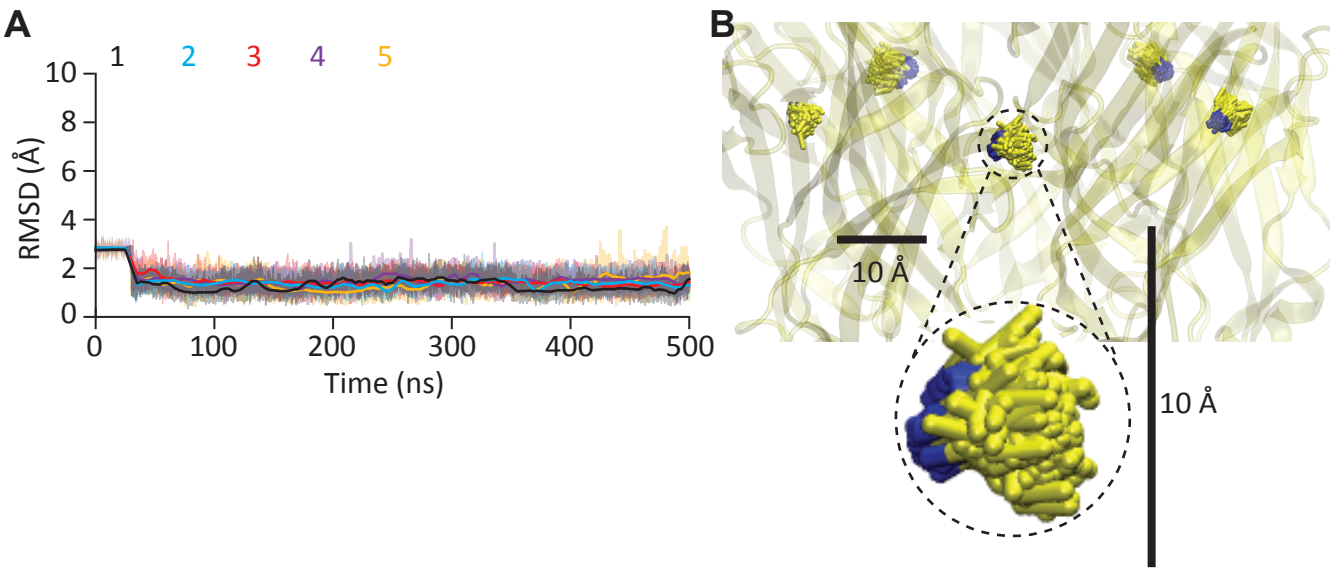

Fig. S8. The orientation of propylammonium in the orthosteric agonist-binding sites. All-atom MD simulation of bound propylammonium starting with a modified version of the agonist-bound atomic model of ELIC: unlike the simulation illustrated in Fig. 7, here, the starting orientation of propylammonium was with the nitrogen atom pointing away from the carboxylates of Glu 77 and Glu 131. (*A*) The heavy-atom RMSD values of each of these molecules, relative to the unmodified atomic model of agonist-bound ELIC, were measured every 10 ps and are displayed (thin lines) using the same *y*-axis scale as in Fig. 7A; thick lines represent moving averages. By the 40th ns of simulation, all five ligands inverted their orientation and pointed their nitrogen atoms toward Glu 77 and Glu 131. (*B*) The five molecules of propylammonium in the 51–500-ns simulation interval are displayed at one frame per nanosecond, in licorice representation. Carbon atoms are colored yellow, and nitrogens are colored blue. The scale bars are the same as those in Fig. 7B. Analysis of these last 450 ns of MD indicated that the root mean-square fluctuation of propylammonium about its mean position (averaged over the five molecules) was 0.6 Å for the nitrogen atom and 1.2 Å for the most distal carbon, that is, exactly the same values as obtained for the simulation that started with all five propylammonium molecules pointing their nitrogen atoms toward Glu 77 and Glu 131 (Fig. 7B). Molecular images were prepared with VMD (49).

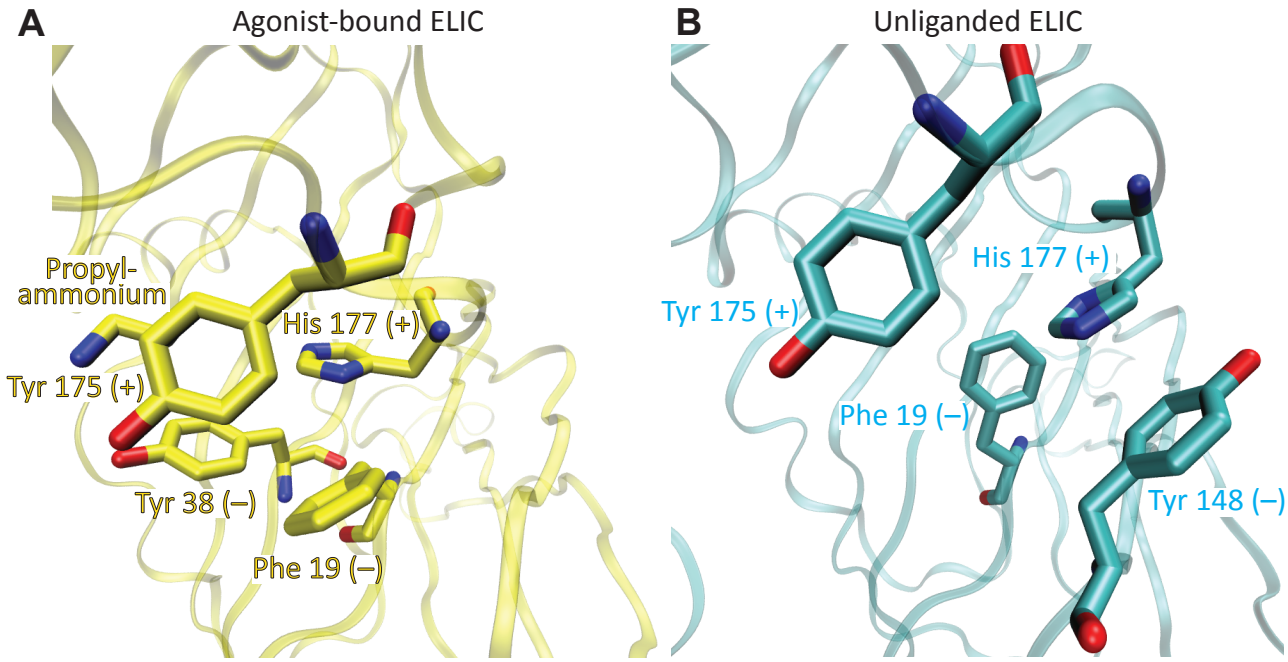

Fig. S9. Aromatic side chains in the microenvironment of loop-C's His 177. (*A*) Propylammonium-bound model. (*B*) Unliganded model. Residues belonging to the "principal" side of the agonist-binding interface are denoted with a "+" sign, whereas those belonging to the "complementary" side are denoted with a "–" sign. Molecular images were prepared with VMD (49).

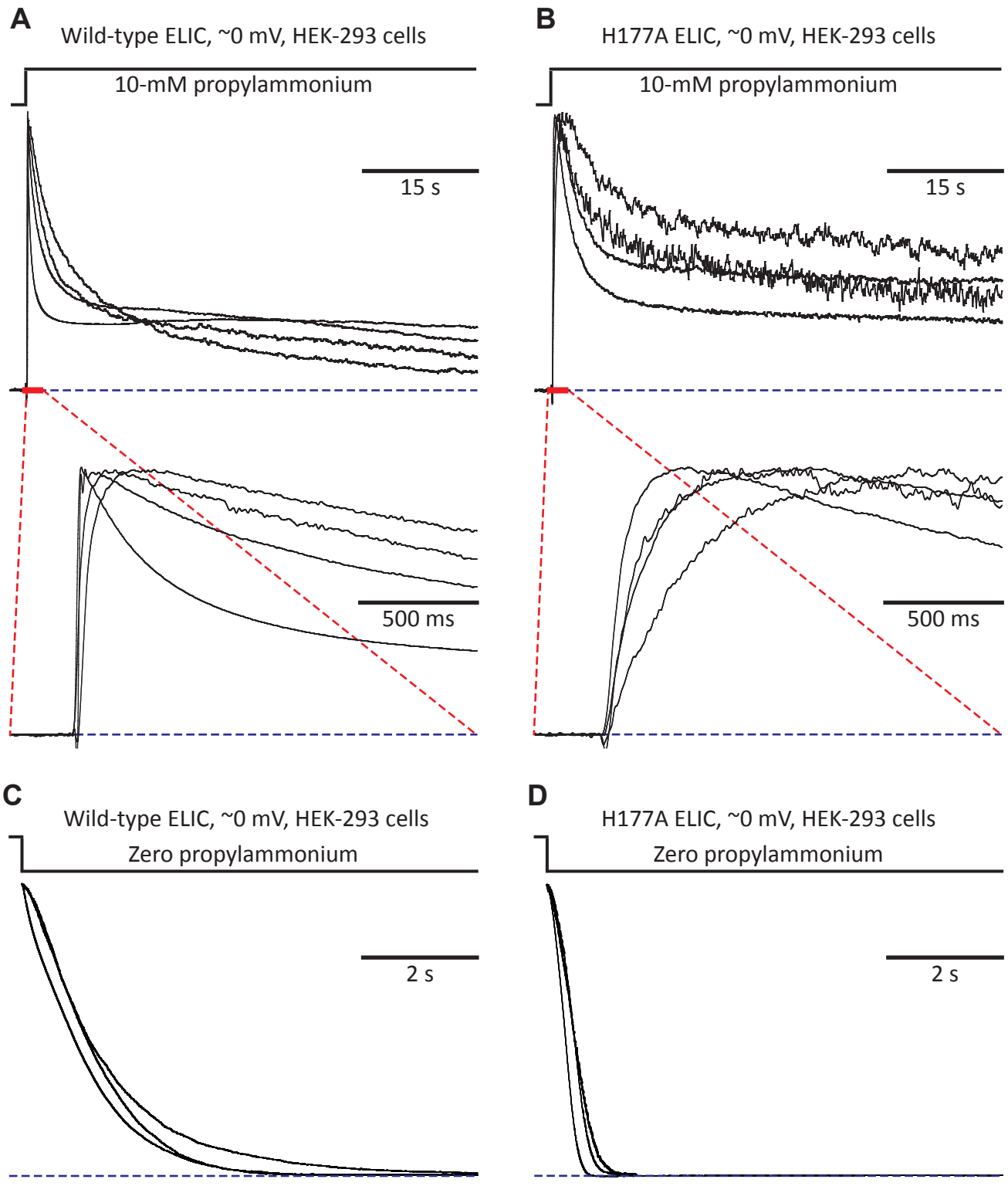

Fig. S10. Functional effect of the H177A mutation. (*A*, *B*) Outward currents recorded under asymmetrical ~150-mM/5-mM (inside/outside) K^+-concentration conditions upon stepping the concentration of extracellular propylammonium from zero to saturating (10 mM). The insets emphasize the activation timecourses. (*C*, *D*) Outward currents recorded under the same K^+-concentration gradient as in *A*, *B* upon stepping the concentration of extracellular propylammonium from 10 mM to zero; the concentration of propylammonium was kept at 10 mM for 20 ms before being switched to zero. Currents in *A*–*D* were recorded from transiently transfected HEK-293 cells in the whole-cell configuration, and the displayed traces are representative of the cell-to-cell variability observed in all of the obtained recordings. In each panel, the traces were normalized to their peak values, and blue dashed lines denote the zero-current baseline. The pipette potential was zero, and the –1.6-mV liquid-junction potential between the pipette and bath solutions was offset; as a result, the membrane potential was close to zero. Each displayed trace was recorded from a different cell.

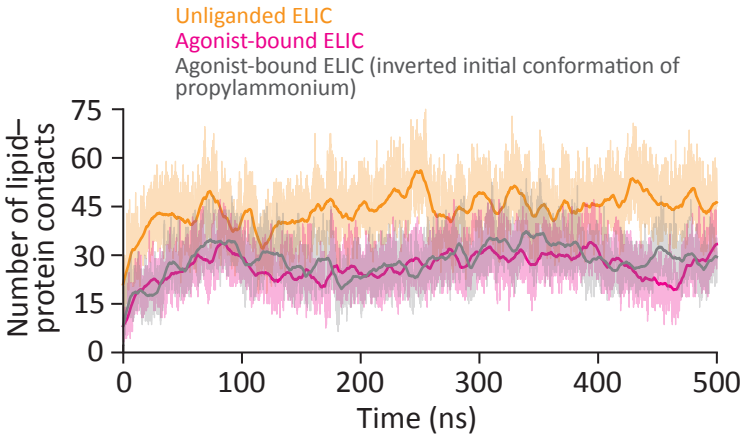

Fig. S11. State-dependent lipid–protein interactions. A contact between lipid and protein was considered to be made if any of the methyl carbon atoms of POPC's choline group was within 4 Å of any of the side-chain oxygen atoms of Asp or Glu, or if any of the oxygen atoms of POPC's phosphate group was within 4 Å of any of the side-chain nitrogen atom(s) of Lys or Arg (50). The analyzed trajectories correspond to the MD simulations in Figs. 7 (agonist-bound), 8 (unliganded), and S8 (agonist-bound with an initially inverted orientation of the agonist). The number of contacts was calculated every 10 ps and is diplayed as thin lines; thick lines represent moving averages. Ionizable side chains were assumed to be in their default protonation states. Reassuringly, the two simulations of agonist-bound ELIC gave very similar lipid–protein-contact profiles.

Table S1. Cryo-EM data-collection, processing, and model-refinement statistics

Sample	Unliganded ELIC in POPC-only nanodiscs	ELIC–propylammonium complex in POPC-only nanodiscs
Data collection		
Grids	Carbon lacey nanowire	Gold lacey nanowire
Vitrification method	Spotiton	Spotiton
Microscope	Krios II	Krios II
Voltage (kV)	300	300
Magnification factor	45,454	45,454
Detector	K2 Summit	K2 Summit
Recording mode	Counting	Counting
Electron-dose rate ($e^{-}Å^{-2}s^{-1}$)	7.6	7.7
Total electron dose ($e^{-}Å^{-2}$)	63.56	63.75
Pixel size (Å)	1.096	1.096
Number of frames	50	50
Total exposure time (s)	10	10
Set defocus range (μm)	1.5–2.2	1.5–2.2
EM-data processing		
Number of micrographs	1,139	1,033
Number of picked particles	289,375	667,903
Number of particles used for refinement	29,207	98,696
Symmetry imposed	C5	C5
Resolution (Å) (half map–half map, FSC threshold = 0.143)	4.1	3.3
Coordinate refinement and validation		
RMSD bonds (Å)	0.007	0.006
RMSD angles (°)	1.025	0.901
Ramachandran favored (%)	90.46	93.18
Ramachandran outliers (%)	0	0
Rotamer outliers (%)	1.82	0.79
Map–model cross correlation (CC, main chain)	0.74	0.82
Clashscore	8.78	3.87
MolProbity score	2.21	1.61
EMRinger score	0.954	3.74
Map–model FSC (Å) (threshold = 0.5)	4.3	3.3

SI REFERENCES

1. Hilf RJ, Dutzler R (2008) X-ray structure of a prokaryotic pentameric ligand-gated ion channel. *Nature* 452:375–3793.
2. Gonzalez-Gutierrez G, Lukk T, Agarwal V, Papke D, Nair SK, Grosman C (2012) Mutations that stabilize the open state of the Erwinia chrisanthemi ligand-gated ion channel fail to change the conformation of the pore domain in crystals. *Proc Natl Acad Sci USA* 109:6331–6336.
3. Ritchie TK, et al (2009) reconstitution of membrane proteins in phospholipid bilayer nanodiscs. *Methods Enzymol* 464:211–231.
4. Keller BU, Hedrich R, Vaz WLC, Criado M (1988) Single channel recordings of reconstituted ion channel proteins: an improved technique. *Pflügers Arch* 411:94–100.
5. Cuello LG, Cortes DM, Perozo E (2017) The gating cycle of a K^+ channel at atomic resolution. *eLife* 6:e28032.
6. Akashi K, Miyata H, Itoh H, Kinosita Jr K (1998) Formation of giant liposomes promoted by divalent cations: critical role of electrostatic repulsion. *Biophys J* 74:2973–2982.
7. Elenes S, Decker M, Cymes GD, Grosman C (2009) Decremental response to high-frequency trains of acetylcholine pulses but unaltered fractional Ca^{2+} currents in a panel of "slow-channel syndrome" nicotinic receptor mutants. *J Gen Physiol* 133:151–169.
8. Razinkov I, et al (2016) A new method for vitrifying samples for cryoEM. *J Struct Biol* 195:190–198.
9. Suloway C, et al (2005) Automated molecular microscopy: the new Leginon system. *J Struct Biol* 151:41–60.
10. Lander G, et al (2009) Appion: an integrated database-drive pipeline to facilitate EM image processing. *J Struct Biol* 166:95–102.

11. Zheng SQ, Palovcak E, Armache JP, Verba KA, Cheng Y, Agard DA (2017) MotionCor2: anisotropic correction of beam-induced motion for improved cryo-electron microscopy. *Nat Methods* 14:331–332.

12. Voss NR, Yoshioka CK, Radermacher M, Potter CS, Carragher B (2009) DoG Picker and TiltPicker: software tools to facilitate particle selection in single particle electron microscopy. *J Struct Biol* 166:205–213.

13. Scheres SH (2012) RELION: implementation of a Bayesian approach to cryo-EM structure determination. *J Struct Biol* 180:519–530.

14. Long F, Vagin AA, Young P, Murshudov GN (2007) BALBES: A molecular-replacement pipeline. *Acta Crystallogr. Sect. D Biol. Crystallogr.* 64:125–132.

15. Emsley P, Lohkamp B, Scott WG, Cowtan K (2010) Features and development of *Coot*. *Acta Crystallogr D* 66:486–501.

16. Adams PD, et al (2010) PHENIX: a comprehensive Python-based system for macromolecular structure solution. *Acta Crystallogr D Biol Crystallogr* 66:213–221.

17. Afonine P, et al (2018) New tools for the analysis and validation of cryo-EM maps and atomic models. *Acta Crystallogr D Struct Biol* 74:814–840.

18. Davis IW, Murray LW, Richardson JS, Richardson DC (2004) MOLPROBITY: structure validation and all-atom contact analysis for nucleic acids and their complexes. *Nucleic Acids Res* 32:W615–W619.

19. Trabuco LG, Villa E, Mitra K, Frank J, Schulten K (2008) Flexible fitting of atomic structures into electron microscopy maps using molecular dynamics. *Structure* 16:673–683.

20. Singharoy A, Teo I, McGreevy R, Stone JE, Zhao J, Schulten K (2016) Molecular dynamics-based refinement and validation for sub-5 Å cryo-electron microscopy maps. *eLife* 5:61–67.

21. Wang Y, et al (2018) Constructing atomic structural models into cryo-EM densities using molecular dynamics – Pros and cons. *J Struct Biol* 204:319–328.

22. Barad BA, et al (2015) EMRinger: side chain-directed model and map validation for 3D cryo-electron microscopy. *Nat Methods* 12:943–946.

23. Schwede T, Kopp J, Guex N, Peitsch MC (2003) SWISS-MODEL: an automated protein homology-modeling server. *Nucleic Acids Res* 31:3381–3385.

24. Biasini M, et al (2014) SWISS-MODEL: modeling protein tertiary and quaternary structure using evolutionary information. *Nucleic Acids Res* 42:W252–W258.

25. Phillips JC, et al (2005) Scalable molecular dynamics with NAMD. *J Comput Chem* 26:1781–1802.

26. Huang J, et al (2016) CHARMM36m: an improved force field for folded and intrinsically disordered proteins. *Nat Methods* 14:71–73.

27. Vanommeslaeghe K, et al (2010) CHARMM general force field: a force field for drug-like molecules compatible with the CHARMM all-atom additive biological force fields. *J Comput Chem* 31:671–690.

28. Vanommeslaeghe K, MacKerell Jr AD (2012) Automation of the CHARMM general force field (CGenFF) I: bond perception and atom typing. *J Chem Inf Model* 52:3144–3154.

29. Vanommeslaeghe K, Raman EP, MacKerell Jr AD (2012) Automation of the CHARMM General Force Field (CGenFF) II: assignment of bonded parameters and partial atomic charges. *J Chem Inf Model* 52:3155–3168.

30. Heath MT (2002) Scientific Computing: An Introductory Survey. (McGraw-Hill, New York).

31. Ghosh A, Sendrovic Rapp C, Friesner RA (1998) Generalized Born model based on a surface integral formulation. *J Phys Chem B* 102:10983–10990.

32. Tsui V, Case DA (2000) Molecular dynamics simulations of nucleic acids with a generalized Born solvation model. *J Am Chem Soc* 122:2489–2498.

33. Allen MP, Tildesley DJ (1987) Computer Simulation of Liquids. (Oxford University Press, Oxford).

34. Wu EL, et al (2014) CHARMM-GUI Membrane Builder toward realistic biological membrane simulations. *J Comput Chem* 35:1997–2004.

35. Gonzalez-Gutierrez G, Wang Y, Cymes GD, Tajkhorshid E, Grosman C (2017) Chasing the open-state structure of pentameric ligand-gated ion channels. *J Gen Physiol* 149:1119–1138.

36. Klauda JB, et al (2010) Update of the CHARMM all-atom additive force field for lipids: validation on six lipid types. *J Phys Chem B* 114:7830–7843.

37. Venable RM, Luo Y, Gawrisch K, Roux B, Pastor RW (2013) Simulations of anionic lipid membranes: development of interaction-specific ion parameters and validation using NMR data. *J Phys Chem B* 117:10183–10192.

38. Martyna GJ, Tobias DJ, Klein ML (1994) Constant pressure molecular dynamics algorithms. *J Chem Phys* 101:4177–4189.

39. Feller SE, Zhang Y, Pastor RW (1995) Constant pressure molecular dynamics simulation: the Langevin piston method. *J Chem Phys* 103:4613–4621.

40. Zwanzig RW (1954) High temperature equation of state by a perturbation method. I. Nonpolar gases. *J Chem Phys* 22:1420–1426.

41. Cournia Z, Allen B, Sherman W (2017) Relative binding free energy calculations in drug discovery: recent advances and practical considerations. *J Chem Inf Model* 57:2911–2937.

42. Liu P, Dehez F, Cai W, Chipot A (2012) A toolkit for the analysis of free-energy perturbation calculations. *J Chem Theory Comput* 8:2606–2616 (2012).

43. Bennett CH (1976) Efficient estimation of free energy differences from Monte Carlo data. *J Comput Phys* 22:245–268.

44. Rosenthal PB, Henderson R (2003) Optimal determination of particle orientation, absolute hand, and contrast loss in single-particle electron cryomicroscopy. *J Mol Biol* 333:721–745.

45. de la Rosa-Trevín JM, et al (2016) Scipion: a software framework toward integration, reproducibility, and validation in 3D electron microscopy. *J Struct Biol* 195:93–99.

46. Vilas JL, et al (2018) MonoRes: automatic and accurate estimation of local resolution for electron microscopy maps. *Structure* 26:337–344.

47. The PyMOL Molecular Graphics System, Version 1.7.2.1 Schrödinger, LLC.

48. Smart OS, Neduvelil JG, Wang X, Wallace BA, Sansom MS (1996) HOLE: a program for the analysis of the pore dimensions of ion channel structural models. *J Mol Graph* 14:354–360.

49. Humphrey W, Dalke A, Schulten K (1996) VMD: visual molecular dynamics. *J Mol Graph* 14:33–38.

50. Barlow DJ, Thornton JM (1983) Ion-pairs in proteins. *J Mol Biol* 168:867–885.